Project No. 10-884

Development of a Scanning Microscale Fast Neutron Irradiation Platform for Examining the Correlation Between Local Neutron Damage and Graphite Microstructure

Reactor Concepts

Dr. Patrick Pinhero
University of Missouri - Columbia

In collaboration with:
Idaho National Laboratory

William Corwin, Federal POC
Will Windes, Technical POC

NEUP Nuclear Energy University Programs
U.S. Department of Energy

NEUP CFP-10-884
FINAL REPORT
12 December 2014
PI: Patrick J. Pinhero
University of Missouri
Columbia, MO 65211

EXECUTIVE SUMMARY

The fast particle radiation damage effect of graphite, a main material in current and future nuclear reactors, has significant influence on the utilization of this material in fission and fusion plants. Atoms on graphite crystals can be easily replaced or dislocated by fast protons and result in interstitials and vacancies. The currently accepted model indicates that after most of the interstitials recombine with vacancies, surviving interstitials form clusters and furthermore gather to create loops with each other between layers. Meanwhile, surviving vacancies and interstitials form dislocation loops on the layers. The growth of these inserted layers cause the dimensional increase, i.e. swelling, of graphite. Interstitial and vacancy dislocation loops have been reported and they can easily been observed by electron microscope. However, observation of the intermediate atom clusters becomes is paramount in helping prove this model. We utilize fast protons generated from the University of Missouri Research Reactor (MURR) cyclotron to irradiate highly-oriented pyrolytic graphite (HOPG) as target for this research. Post-irradiation examination (PIE) of dosed targets with high-resolution transmission electron microscopy (HRTEM) has permit observation and analysis of clusters and dislocation loops to support the proposed theory. Another part of the research is to validate M.I. Heggie's *Ruck and Tuck* model, which introduced graphite layers may fold under fast particle irradiation. Again, we employed microscopy to image irradiated specimens to determine how the extent of *Ruck and Tuck* by calculating the number of folds as a function of dose.

Our most significant accomplishment is the invention of a novel class of high-intensity pure beta-emitters for long-term lightweight batteries. We have filed four invention disclosure records based on the research conducted in this project. These batteries are lightweight because they consist of carbon and tritium and can be fabricated to conform to many geometric shapes. In addition, we have published eight peer-reviewed American Nuclear Society (ANS) transactions, and presented our findings at ANS National Meetings, and several universities.

BACKGROUND:

The increasing demand of energy has lead to the current *energy security* crisis. Despite significant pressures to decrease the production and use of fossil fuel, most of the fast-growing energy demand is still being satisfied by fossil fuel. Some of these pressures are founded in environmental concerns like significant air pollution, for example, dust, heavy metals, NO_x and SO_x; and the generally accepted global warming problem caused by the production and release of greenhouse gases. In order to solve the energy crisis in an environmental friendly way, a clean and sustainable energy is needed.

Many renewable energy solutions, such as tidal, wind and solar have varying limitations and thus are not able to provide continuous electricity continuously and reliably. Hydropower has strict demand on terrain, specifically the potential energy drop over the generator turbines bridging the flow. Nuclear energy has great potential as an option to meet people's demands on energy, and maintain global climate sustainability. Accordingly, nuclear energy is anticipated to play an important role in the future energy supply in a safer, more environmentally clean, and more economic manner. Besides, the output of nuclear technology has great market. United States has 100 nuclear plants and a large number of them need replacing while China has 20 nuclear plants in operation, 28 under construction and more about to start construction. Additionally, India, Russia, and countries in South America also have interests in building more nuclear plants.
Generation IV (Gen IV) reactors are next generation nuclear plants, being researched as the next evolution of more reliable, safer, and economically sound. As a result, six potential designs are proposed to meet these guidelines.

The very-high temperature reactor (VHTR) is the principal Generation IV reactor design under consideration in the Unites States. The VHTR is a graphite-moderated nuclear reactor with a once-through uranium fuel cycle[1]. The VHTR is considered to be a promising candidate for the production of both electricity and process heat. As we know, moderators in nuclear reactors are used as medium to slow down the fast neutrons, and further transform them into thermal neutrons to sustain nuclear chain reaction[2]. The proposed VHTR features an outlet temperature for more than 1000°C. High temperature and neutron irradiation on the graphite can result in various radiation damage defects and structural changes on graphite material. High temperature will accelerate the radiation damage, so the graphite in the VHTR must not undergo a very fast structural change which could have an unexpected impact on the operation of entire nuclear reactor system[3].

The study of neutron radiation damage on graphite provided a way to understand the behavior of graphite in the nuclear reactor under certain circumstances and it will be useful for the future design and operation of VHTR. This study mainly focused on irradiation simulation of graphite in VHTR, irradiation of the sample with fast particles and acquisition of microscopic images on the irradiated graphite samples. The simulation included the estimation of the ion trajectories to fast particles and collision events happened within the sample, along with the calculation of displacement per atom (dpa) of the radiation material. By conducting fast particle irradiation on the graphite sample, structural changes will have already taken place on the sample. With observations upon

microscopy, including electron microscopy and atomic force microscopy, surface topography and dislocation defects will be measured.

The initial step of the experiment was at room temperature during irradiation. We will increase temperature in the future experiments. To introduce more particle energy to the material and irradiate as energetic particle as in the nuclear reactor, it is much easier to substitute the neutrons with protons. Protons can be generated in cyclotron with high energy. Meanwhile, protons and neutrons have similar momentum because the mass of them is similar. We employed the GE PETtrace Cyclotron at University of Missouri Research Reactor (MURR) to produce fast protons with 16.5 MeV. The actual energy irradiated at the sample will be slightly lower than the value at the beam port. This will further discussed in the experiment chapter.

After the irradiation, microscopy was used to analyze the structural changes, especially creation and aggregation of massive point defects, the movement and coalescence of basal point defects and atomic clusters, as long as morphology change of surface and sub-surface area by fast particle irradiation. In the future, suggestions on the design and operation of nuclear reactor can be provided based on more data on the behavior of graphite under circumstances of high temperature and neutron radiation.

While the cyclotron is operating, H^- ions are extracted out of an ion source in the middle of the cyclotron. Magnetic fields are applied to the negatively charged ions, causing them to travel in a circular path within the cyclotron. A RF electric pulse accelerates those ions to increase the radius of their circular path due to the following equation:

$$r = \frac{m\boldsymbol{v}}{q\boldsymbol{B}} \tag{1}$$

where r stands for the radius of their circular path, m, **v**, q and **B** are mass, velocity, charge of the particle and magnetic field respectively. Once the radius is large enough and the orbit of those particles are near the exit of the cyclotron, those negatively charged ions strike a stripping foil, which convert those negatively charged particles to positive protons (H^+). The magnetic force can be calculated in the following equation:

$$\boldsymbol{F} = q(\boldsymbol{E} + \boldsymbol{v} \times \boldsymbol{B}) \tag{2}$$

where F stands for magnetic force, q, **E**, **v** and **B** are particle charge, electric field, particle velocity and magnetic field respectively. The exit is assumed to be field free. Because the charge of particles changed from negative to positive, this acts to place an internal force on the beam which ejects the protons out of the cyclotron into a beam transport tube. The beam port we are using is beam port 2. One stripping foil can accurately extract the cyclotron beam out of this beam port. A schematic of a GE PETtrace Cyclotron is shown in Figure 1.

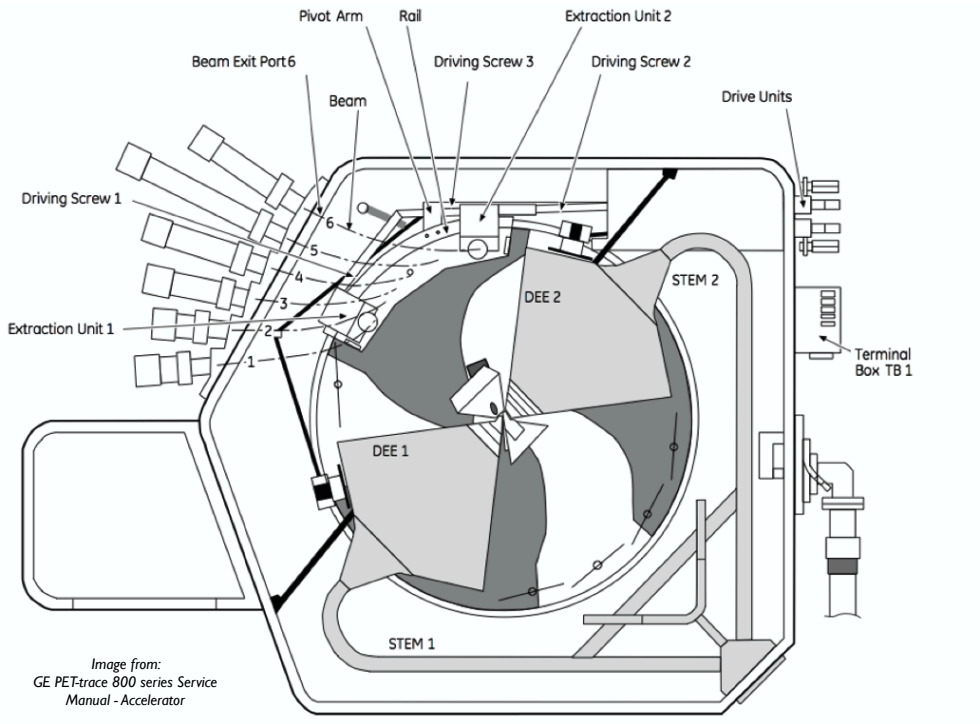

Figure 1 A schematic of a GE PETtrace cyclotron

We connected the beam port of the cyclotron and the sample target with a aluminum tube. In order to ensure the safety of experimenter and other equipment attached to the system, for example, a mechanical pump and an oil diffusion pump was planted underneath the sample chamber, and a lead shielded concrete cinder block wall was constructed at around 3 meters away from the cyclotron to shield the experimentation team from gamma-radiation dose. The beam traverses another 1.5 meters from the wall to the chamber, the beamline travels approximately 4.5 meters in the tube. Particle beams always have a velocity component perpendicular to their primary motion direction because of the same charge particle pulse and particle random thermal motion. As a result, the beamline expands as it travels through this distance[4]. This expansion is known as beam divergence, shown in Figure 2.

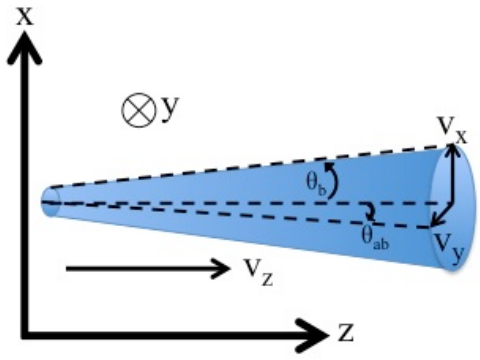

Figure 2 Diagram of the beam divergence

Quadrupole magnets are an ideal way to focus the beamline. By applying different magnetic fields on these three quadrupole magnets, the expanded beamline will be focused to a point. This design, simulation and installation of quadrupole magnets were done [5], so there is no need to discuss this further about the mechanism of quadrupole magnets in this thesis. The quadrupole magnets are shown in Figure 3.

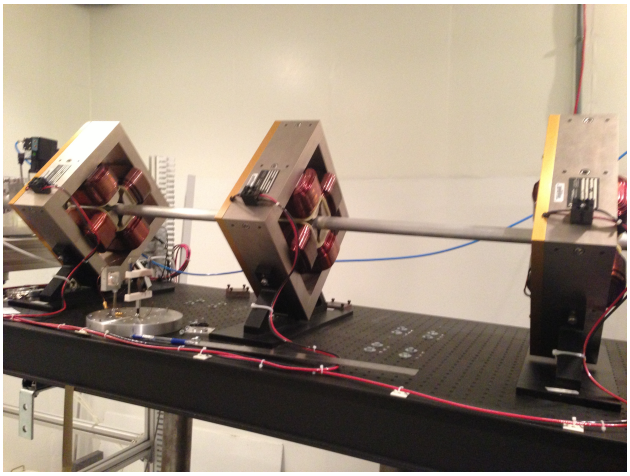

Figure 3 Picture of quadrupole magnets

A schematic of beamline system is shown in Figure 4 and the numerical legend is shown in Table 1.

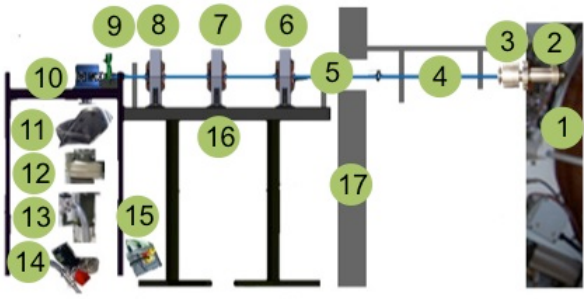

Figure 4 A schematic of beamline system [5]

Table 1 Table of content of beamline system [5]

Component	Tag #
cyclotron	1
KF40 cyclotron adapter	2
collimator	3
short drift tube	4
long drift tube	5
quadrupole #1	6
quadrupole #2	7
quadrupole #3	8
VAT Valve	9
vacuum chamber and table	10
gate valve	11
liquid nitrogen baffle	12
oil diffusion pump	13
mechanical pump	14
solid-state relay box	15
breadboard table	16
concrete wall	17

After the protons exited the cyclotron from beam port, they travel through a series of drift tubes where quadrupole magnets were installed to focus the beamline. The sample was mounted in the chamber that connected to the drift tubes. A mechanical pump and an oil diffusion pump were used to evacuate the chamber system. The base vacuum the is less than 10^{-7} torr. A Neslab RTE-9DD chiller was used to cool the oil diffusion pump. The current of quadrupole magnets were provided by 3 separate power supplies controlled through a LabView program. A TerraNova pressure controller was used to monitor system pressure and to assure that the chamber is maintained at $< 10^{-5}$ torr.

The experiment was operated and logged remotely using a laptop on which was installed with LabView, the Neslab chiller, power supplies, and pressure control in an adjacent lab external to the cyclotron vault. The wall between the lab and cyclotron vault is 6 feet thick poured concrete to protect the experimentalist from radiation dosing. The procedures to operate the beamline system and conduct radiation experiment are included in the appendix.

Theoretical studies of graphite radiation damage started from the early 1960s in order to understand the damage to the graphite moderators in the early nuclear plant[6]. In general, creation and aggregation of a significant number of point defects, which change the surrounding graphite layers results in the radiation damage in graphite. The damage can cause significant material property change, including elasticity, mechanical strength, conductivity, and creep behavior[7]. This research area continues to spak interest because it will greatly benefit fission reactor design, and potentially have bearing on fusion reactor development. This thesis will mainly focus on the creation and aggregation of point defect.

An atomic displacement happens when an incoming energetic particle hit the crystal lattice where the kinetic energy transferred onto the layer exceeds the binding energy[7]. The displaced atom, known as primary knock-on atom (PKA) is knocked out of the site. The PKA may further collide with other atoms and form atomic displacement cascade, shown in Figure 5, if they have enough energy. Secondary knock-on atoms may further be knocked out if they remain to be energetic enough to overcome the binding energy holding them in their lattice position.

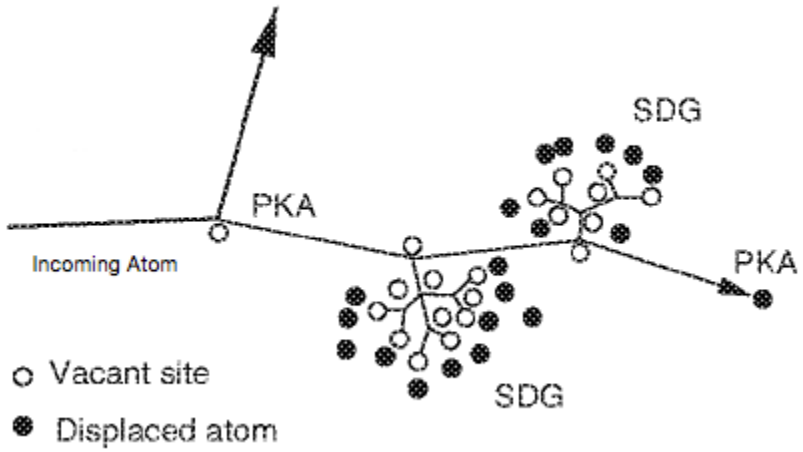

Figure 5 Schematic of atomic displacement cascade of PKA and the first group of secondary displacement groups (SDG)[7]

As a result, a large amount of atoms will be knocked out of their sites and transported to other positions in the graphite matrix. The knock-on graphite atom will create a vacant site (vacancy) where it originally resided. Therefore, knocked-on atoms are expected to form interstitials or recombine with vacancy (vacancy annihilation) to reform a semblance of the original stable structure. The remaining knocked-on atoms form stable interstitial atomic clusters with other knocked-on atoms[8]. A combination of the interstitial defect and a vacancy defect are called a *Frenkel Pair*.

The interstitial atomic clusters created by a few atoms are intended to move in the spacing between graphite layers and further coalesce with each other and form interstitial dislocation loops. An interstitial dislocation loop is a structure, which is more stable than single isolated atomic clusters because its mass is much greater than single clusters and thermodynamics, i.e., interparticle bonding . The structure of a dislocation loop is shown in Figure 6, in which the coalescent of interstitial atomic clusters reached a significant size and form a new layer inserted between two existing layers.

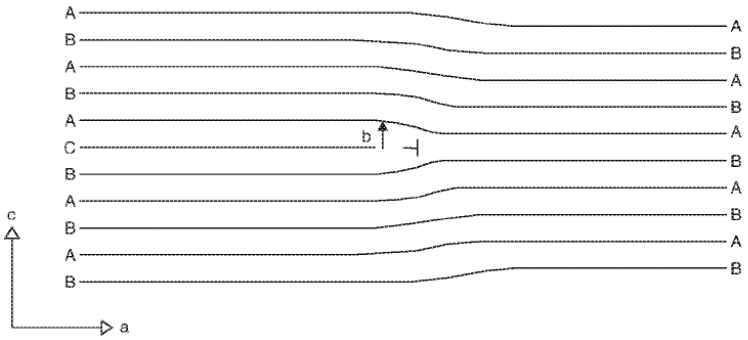

Figure 6 The structure of dislocation loop

Vacancy defects are intended to move together and form vacancy dislocation loops. However, the migration energy of vacancies is greater than the migration energy of interstitials, so vacancies are usually not as mobile as interstitials. This results in the size of vacancy dislocation loops being often smaller than the size of interstitial dislocation loops[9].

The weak bonds between adjacent HOPG layers along the prismatic direction make it easy to buckle, winkle and fold the structure. Fast proton irradiation induces quite a large number of basal dislocations initially, which are able to mutually interact with each other and freely expand, leading to sa “pile up”. These “pile up” happen on the same layer and they become layer folds. As the schematic of basal dislocations pile up as shown in Figure 7, dotted lines represent the graphene layers. Four basal edge dislocations are piled up on the each side of the same folded layer. Basal edge dislocations on one side of the fold structure glide past each other and climb onto the other side of the fold structure via point defect migration, and increase the size of fold structure. Continued radiation helps grow the folded part and eventually turns into the *ruck and tuck* structure[10]. The mass increased in the folded layer comes from the radiation source. However, there is a maximum width of the folded layer because, within the folder layer, it becomes more difficult for climb dipoles, which are basal dislocations lined up on either side of fold structure, to switch onto the other side especially when more layers fold simultaneously[11].

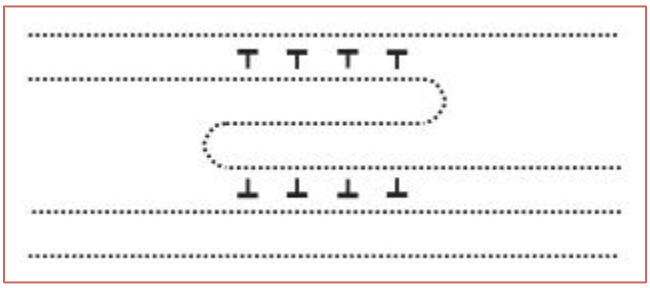

Figure 7 Schematic of basal edge dislocation pile up

The formation of *ruck and tuck* will induce a dimensional expansion of c-axis, i.e., the axis parallel to the prismatic plane and normal to the basal plane. On a larger, more

macroscopic scale, the formation of *ruck and tuck* usually happens in the same x-y region, where it is very easy to accumulate dimensional expansions and make it easy to observe.

As an alternative, it is also possible that the inserted layer formed by interstitial clusters increase the dimension on the *c*-axis. Small interstitial defect clusters can substantially change the spacing between layers. However, the location of interstitial clusters are scattered (stochastically distributed) and none of the defect cluster structure are able to account for large amount of dimensional change[10].

Graphite is an allotropic form of carbon, which contains a large volume of defects. Pyrolysis of organic compounds is a common way to perfect the structure of graphite. Pyrolytic graphite is a high-degree preferred crystallographic orientation, in which the *c*-axis is perpendicular to the substrate surface. Highly Oriented Pyrolytic Graphite (HOPG) can be obtained by annealing pyrolytic graphite under compressive stress and temperature at about 3300K. The crystal structure of HOPG is characterized by an arrangement of ABAB stack of graphene layers. The spacing between each layer is 0.335nm. It is an idealistic material for scanning probe microscopy as a substrate because it has an extremely smooth and flat surface and it is easily renewable by using scotch tape to cleave. Mosaic spread is used to measure the parallelism of grain boundaries. The lower the mosaic spread, the higher the order of HOPG is. Cleaving by scotch tape is common to process HOPG before experiment[12]. HOPG is one of the most anisotropic carbon-based materials. It is often chosen to be the material to study the processes under ion and neutron irradiation[13][14].

The study of penetration of a particle into matter and the particle slowing in the matter started a long time ago. However, with increasing complexity of describing the ion and target interactions, it is more difficult to study them. The *Stopping and Range of Ions in Matter (SRIM)* is a group of computational Monte-Carlo particle trajectory programs used to calculate physical quantities related to different interaction of ions with matter[15]. It was freeware developed by James F. Ziegler and Jochen P. Biersack[16] and been continuously upgraded. It is based on the Monte Carlo simulation method and all the particles start at the same initial position, with same angle and energy. As the output, it plots and lists the three dimensional distribution of ions in the solid, concentration of collision event and energy loss.

Particles with positive or negative charge irradiating matter can be simulated. It has a large material database of material so it is very easy to use. However, neutron irradiation is not available to simulate with this program because the neutron is electric neutrality.

EXPERIMENTAL:

All sample irradiations were carried out at University of Missouri Research Reactor (MURR). Protons generated by the cyclotron act as the radiation source. A set of samples was irradiated for periods ranging from 1 to 9 hours. The direction of the radiation is along the *z*-axis of HOPG sample, i.e. normal to its basal (hexagonally-structured) plane. Post-irradiation examination was completed using transmission electron microscopy (TEM) using a JEOL 1400 TEM operating at 120kV. High resolution TEM (HRTEM) imaging was performed using a FEI Tecnai F30 Twin TEM operating at 300kV. All scanning electron microscopy (SEM) imaging was performed using a FEI Quanta 600 ESEM operating at 5kV. Focused Ion Beam (FIB) lift-out of TEM specimens was performed using a Helios NanoLab 600 dual ion beam gun at 30kV. In addition, all atomic force microscopy (AFM) imaging was performed using Agilent 5400 SPM system in contact mode. SEM, TEM and HRTEM images were acquired at the electron microscopy core (EMC) facility at University of Missouri (MU), AFM images were acquired in Pinhero Lab facilities at MU, and FIB Lift-out were acquired at Missouri S&T University (MST).

After the radiation platform is set up, beamline alignment is necessary to make sure that the target sample is irradiated with the proton beam. This original procedure was work completed prior [5]. In order to double check the beamline alignment, we repeated his alignment work and rechecked the alignment regularly.

Radio-chromic film was inserted at each tube connection and the cyclotron was operated for 5 seconds. If the tube is well-aligned, there should be a tiny beam burn at the center of the film. Figure 8a shows the irradiated at the cyclotron beam port, figure 8b shows the irradiated film at the tube connection at wall and film 8c shows the irradiated film at the connection between tube and sample chamber. As can be observed, films in figure 8a possess a very clear radiation center, which indicates that the proton neam is very well-focused. After adjusting the tube several times and the films in figure 8b were acquired. These become more out of focus compared to figure 8a because of the beamline expansion, however, it is still acceptable. The films in figure 8c have a wider burned area than films in figure 8b. To compensate, the quadrupole magnet currents were adjusted in order to minimize the beamline size. A final alignment step was performed at the location of sample to make sure that the beamline irradiated at the sample is well-aligned and focused.

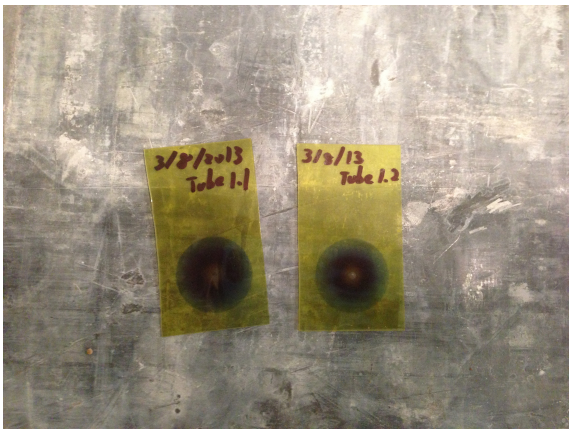

Figure 8a Irradiated film at the beam port

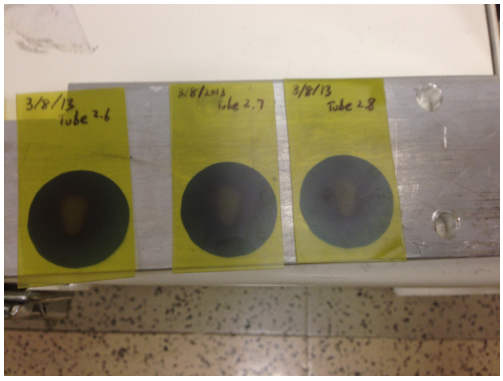

Figure 8b Irradiated film at the tube connecting point near the wall


Figure 8c Irradiated film at the connecting point between tube and sample chamber

Both the tube angle and quadrupole magnets have influence on the beamline alignment. Testing the alignment on the tube connection makes sure that the tubes incline at a proper angle. The current of each of the quadrupole magnets are simulated via SIMION and the alignment validated the simulation result.

The final step alignment was to put the radio-chromic film into the sample chamber and run the cyclotron for 5 seconds. Figure 9 shows the irradiated film in the sample chamber. The white burn on the film indicated the location and size of the beamline, which will bombard on the sample during the experimental process. The diameter of the beamline is about 5 mm.

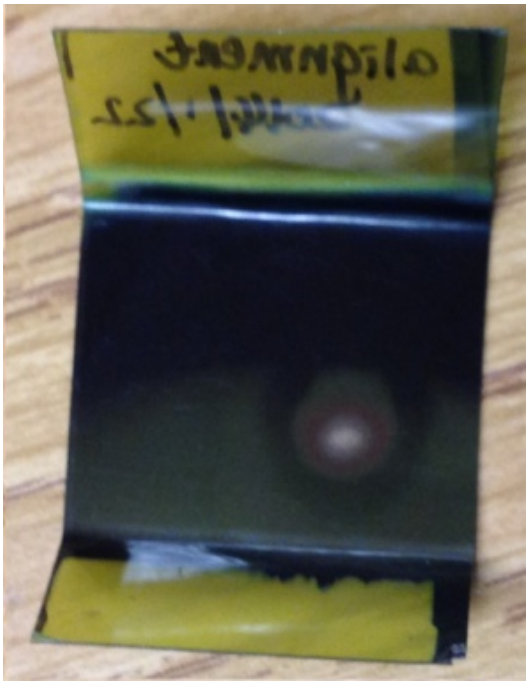

Figure 9 Irradiated film in the sample chamber

In the experiment, the emission current of protons exiting the cyclotron is 20μA. The sample chamber was about 4.5 meters away from the cyclotron beam port. Each proton bombarded at the target travelled through the tube. However, the beam expansion and divergence effects enlarged the beamline and some of the protons collided at the walls of the beamline tube. As a result, not all of the particles were delivered and hit the sample. A faraday cup was fabricated to measure the current of the beamline so that we could further accurately determine the number of particles irradiating the specimen. The faraday cup was machined in the machine shop within the MU College of Engineering. An image of the faraday cup is shown in Figure 10.

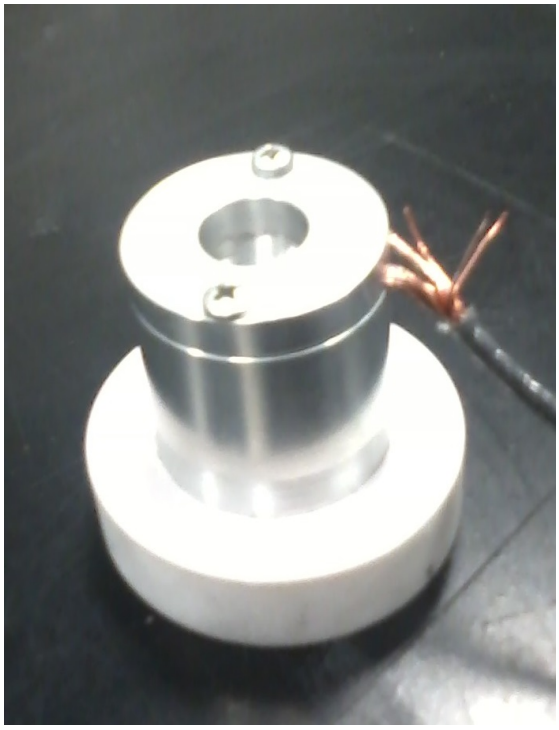

Figure 10 Image of faraday cup used to measure beamline current

The faraday cup is made of aluminum with a ceramic jacket, also along with an aluminum cap. During the measurement, the faraday cup was placed on the sample mount where the opening side is right against the beamline. A wire was connected to the metal material of faraday cup on one end, while the other end attached to a Keithley picoampemeter to monitor the current in the faraday. The ceramic jacket of the faraday cup contacted the metal mount so that current will not be grounded through the mount. It ensures all the current to go through the Keithley picoampemeter.

The beamline has very high energy, which provides them have a very high velocity. The inside of the faraday has a core cave structure and the diameter of the faraday cup cap is much less than the diameter at the top part of core structure, as shown in the Figure 11. This structure ensures the energetic particles to bounce back and forth within the core structure and eventually transmit to picoampemeter rather than bounce back without capturing everything.

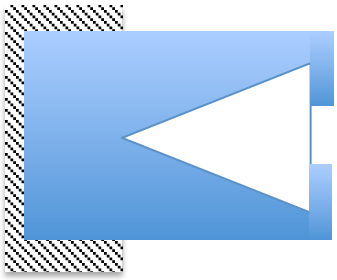

Figure 11 Cross-section image of faraday cup

After we turned on the cyclotron, we were able to read the current from the picoampemeter.

As the beamline travel through the tube, it loses energy because of the residual molecules. In addition, the magnetic force applied on the particles by quadrupole magnets also contribute to the change of beamline energy. A method developed by Tárkányi[17] can be used to measure the energy to beamline. Natural nickel has several different isotopes: 68.27% ^{58}Ni, 26.10% ^{60}Ni, 1.13% ^{61}Ni, 3.59% ^{62}Ni, and 0.91% ^{64}Ni[18]. The proton reaction on the cross-sections causes the change of distribution of nickel isotopes; especially generate ^{57}Ni, ^{55}Co, ^{56}Co and ^{57}Co. To monitor the change to isotopes of nickel by measuring the gamma emitted by the decay of ^{57}Ni, ^{55}Co and ^{57}Co can be used to determine the beam energy.

A nickel foil of the dimensions 20mm × 20mm × 0.1mm with a purity of 99.99% was placed in the sample chamber and it is irradiated for 10 minutes. The beamline current we used for energy measurement is 10 μA. After the irradiation, the nickel foil was moved to a γ detector where the amount of ^{57}Ni, ^{55}Co and ^{57}Co can be measured.
However, the emitted gamma ^{55}Co and ^{57}Ni is much higher than ^{57}Co. For this reason[19], using the ratio of ^{55}Co and ^{57}Ni is an effective way to determine the beam energy. We measured the ratio of ^{55}Co and ^{57}Ni in the nickel foil and compared it with the theoretical data to get the beamline energy.

Samples of HOPG (ZYB grade, produced by NT-MDT Company) have the form of square sheet with side lengths of 10mm and thickness of 1.2mm. The mosaic spread is specified to be in the range of 0.8-1.2 degree and thickness variance is ±0.2mm. Each sample was cleaved at atmospheric pressure and room temperature with the ubiquitous "scotch tape" method, and then mounted into the vacuum chamber, which was connected to the cyclotron as described previously.

SEM is a commonly used electron microscopy technique in material science characterization. It produces images of the sample surface by scanning it via a focused electron beam. The interaction of electrons with atoms on the sample produces signals that contain surface topography and sample composition information. The sample has to be conductive to emit signals on the surface and composition.

Compared to SEM, TEM utilizes a more energetic electron beam gun and the beam is transmitted through the sample. The sample on the TEM has to be ultra-thin to let the electrons pass through. As a result, the resolution of TEM is greatly increased.
HR-TEM is an imaging mode of TEM, which has even higher resolution than regular TEM. The FEI Tecnai F30 HR-TEM we used in EMC possesses a theoretical point resolution of 0.1nm. It is a powerful instrument to image the atomic structures on the material.

Samples need to be moved onto a TEM grid and then the TEM grid will be put into the instrument for microscopy. In order to transmit the electrons through the sample, they will need to be as thin as possible.

However, it is very hard to thin the HOPG samples of interest to this study. In order to accomplish this, scotch tape was glued onto the surface of the sample. By peeling the scotch tape, significant amount of layers could be removed from the sample. Subsequent scotch tape peals from the prior tape resulted in the recovery of a sample to image.. The sample was thinned in this matter to approximately 100-200nm after a few peals.
Although the sample was thinned, it was very difficult to move it onto the grid. In order to remove the sample from the scotch tape, additional sticky grids were used to tremove the sample. These were submerged in about 15ml acetone. Acetone was able to dissolve the glue from the scotch tape but the reaction is very slow. To accelerate the dissolving and make sure the glue was dissolved before the acetone was dried out, tweezers were used to scratch the glue off the tape and discarded the tape afterwards. After these procedures, the solution became sticky. The sticky grids were then placed on a piece of filter paper and dropped the sticky solution onto them. After the grids were dried, drops of the sticky solution were checked to make sure that the grid was sticky enough to remove the glue off the sample. By attaching the sticky grid on the thinned sample, a small amount of sample could be removed to the grid and they could be used in TEM and HR-TEM.

AFM is a type of scanning probe microscopy. It uses a tip to scan the surface topography of samples and output the height of the sample. The resolution of AFM can reach the order of fractions of nanometers.

Contact mode and tapping mode are two different probes to be used. In this experiment, all the AFM images are provided under contact mode.

An FIB setup resembles a SEM and sometimes it is installed as a secondary ion beam gun onto an existing SEM workstation. Instead of using electrons, the FIB uses ions to image the sample. The mass of ion particles is much greater than electrons, so FIBs are destructive to the specimen. As a result, it can be used to lift out a thin TEM specimen from a sample.

Figure 12 a-g shows the steps of doing FIB lift out. The images shown in Figure 12a-e and Figure 12h were acquired within this original work., Figure 12f is cited from the Department of Material Science at Oregon State University and Figure 12g is cited from Arizona State University to help better explain the steps. Pictures were taken by electron beam and the cutting is finished by ion beam.

In Figure 12a, an area was selected that possessed a significant defect as the region of interest. Platinum (Pt) was then deposited in the form of a strip,, as shown in Figure 12b, to protect the region of interest from gallium ion implantation and damage. A trench was milled to isolate the region of interest from each side, as shown in Figure 12c-d. We could see that the amorphous material was deposited to the edge of the trench by the Gallium ion beam, so we need to clean the cross-section before lifting the region of interest out of the sample. Figure 12e shows the image of cleaned cross-section. As shown in Figure 12f, we did a u-cut on the sample. After the u-cut, most of the areas is free except a bridge shape is still connected to the region of interest to support it. We

inserted an OmniProbe and approached it towards the sample. We then deposited platinum onto the probe and sample to connect them. After we make sure that they are connected, we cut the region of interest free. Now the thin film was attached to the OmniProbe, as shown in Figure 12g. We moved the OmniProbe towards an OmniGrid and connected the sample to the OmniGrid at two bottom corners with platinum. After we made sure the sample is on the OmniGrid, we disconnect the sample and OmniProbe. Further cleaning and thinning was required to get rid of the amorphous matters on the sample[20].

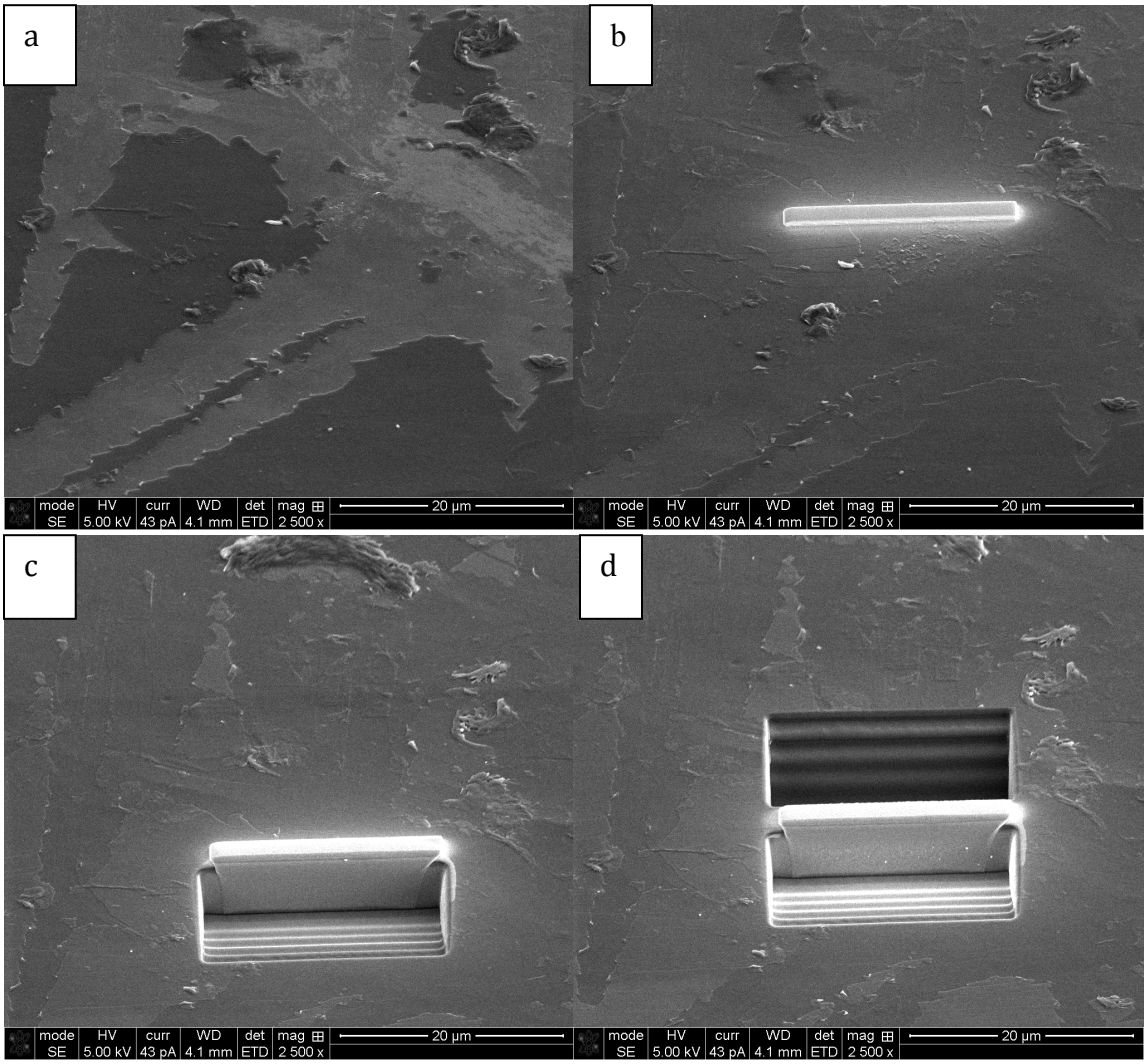

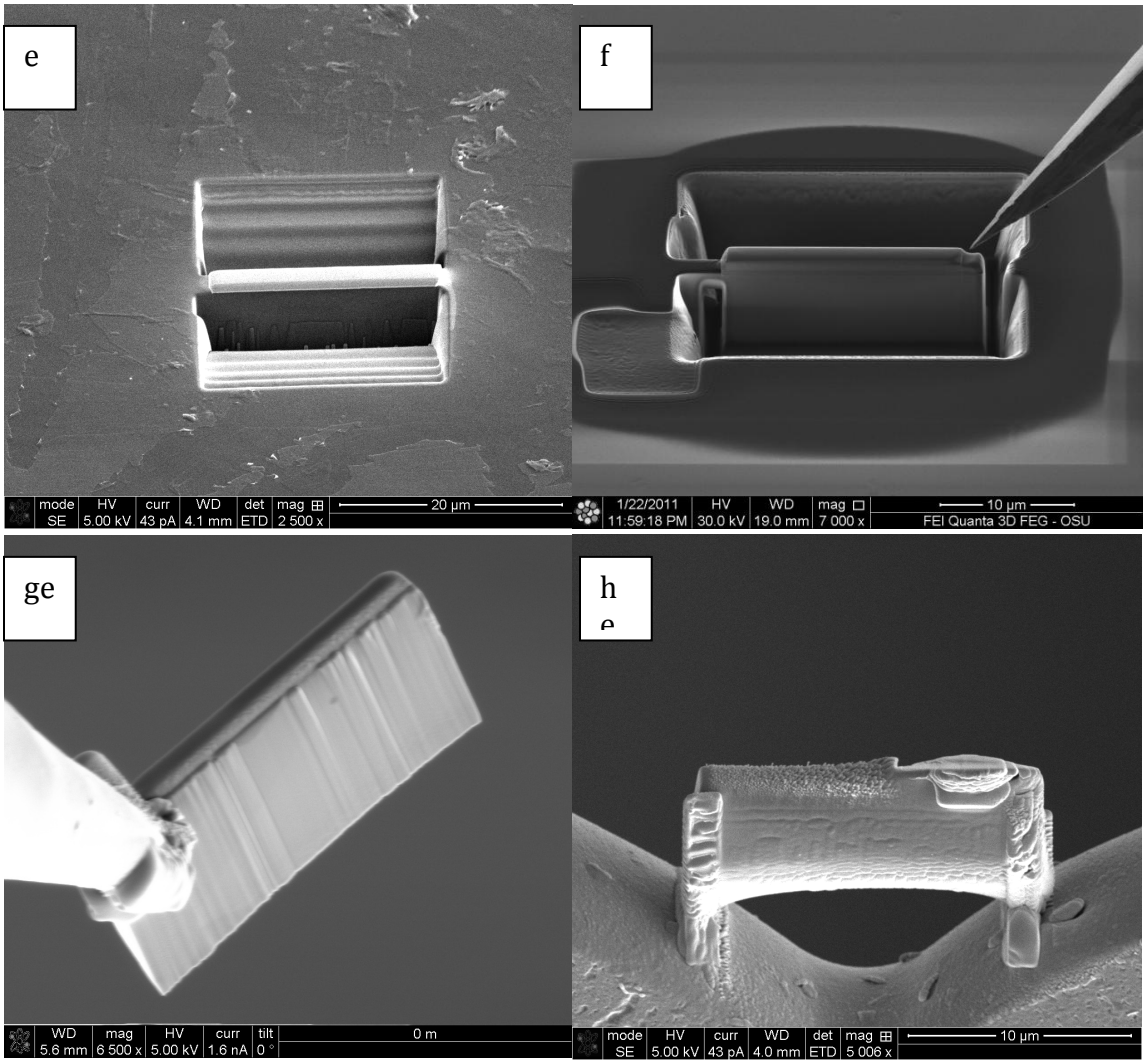

Figure 12a-h Images shows the procedures of FIB lift out

Graphite samples are difficult to thin according to the behavior during the thinning. It is also very easy to roll under high thinning current. As a result, we thinned the sample for 3 times after we attached it to the OmniGrid. The final sample is shown in Figure 13 and the thickness of it is about 100nm. The parameters of ion beam in the thinning process are provided in Table 2.

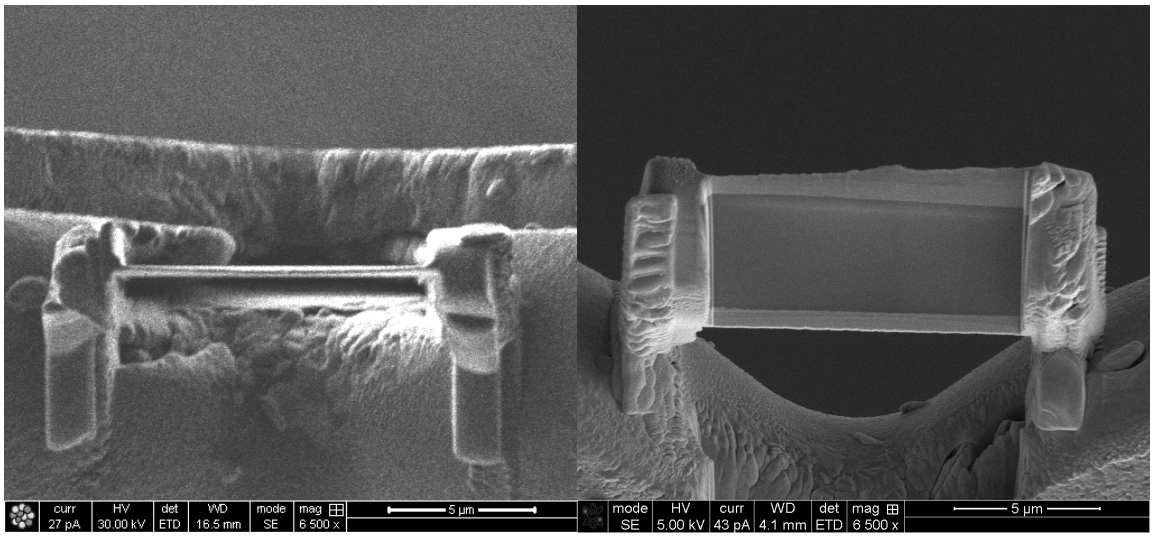

Figure 13 Images of final thinned FIB lift out sample

Table 2 Parameters of ion-beam during the FIB lift out

Ion beam voltage	30kV
Pt deposition current	93pA to 0.28nA
Trenching	6.5nA
Rectangular cleaning	2.8nA
Trench cleaning	0.92nA
U-cut	2.8nA
First final cleaning	93pA
Second final cleaning	48pA
Third final cleaning	28pA

RESULTS:

Displacements per atom (dpa) is the number of times that an atom is displaced for a given fluence of radiation. Dpa can be calculated by the following equation:

$$dpa = \frac{R_d t}{N} = \frac{N\sigma_d(E_p)\varphi(E_p)t}{N} = \sigma_d(E_p)\varphi(E_p)t \quad (3)$$

In the equation 3, R_d represents the rate of atomic displacement. It is proportional to the number of target atoms per volume (N) and the displacement cross-section (σ_d) for particles with energy Ep. The t in the equation 3 represents time. The ion fluence φ is defined as:

$$\varphi = \frac{number\ of\ ions}{St} \quad (4)$$

The S in the equation 4 is the area of cross-section. As is mentioned prior, the beam is focused to a circular size with a diameter of 5mm. The cross-section is the area of this circle, which is 0.2cm^2. Number of ions can be calculated as:

$$Number\ of\ ions = \frac{It}{q} \tag{5}$$

Taking the beam current as 0.6μA, and charge per particle, 1.6×10^{-19} to the equation 5; one can calculate the number of ions per second is 3.75×10^{12}. So the ion fluence φ is 1.875×10^{13} ions/(cm^{2}s).

SRIM can be used to simulate the displacement cross-section. One does this by supplying as input the mass, charge of a proton, the mass of carbon matter, the thickness of the target and set the running time to be 10,000 trajectories. One obtains the collision event plot, as shown in Figure 14, which represents the numbers of vacancies per angstrom-ion versus target depth.

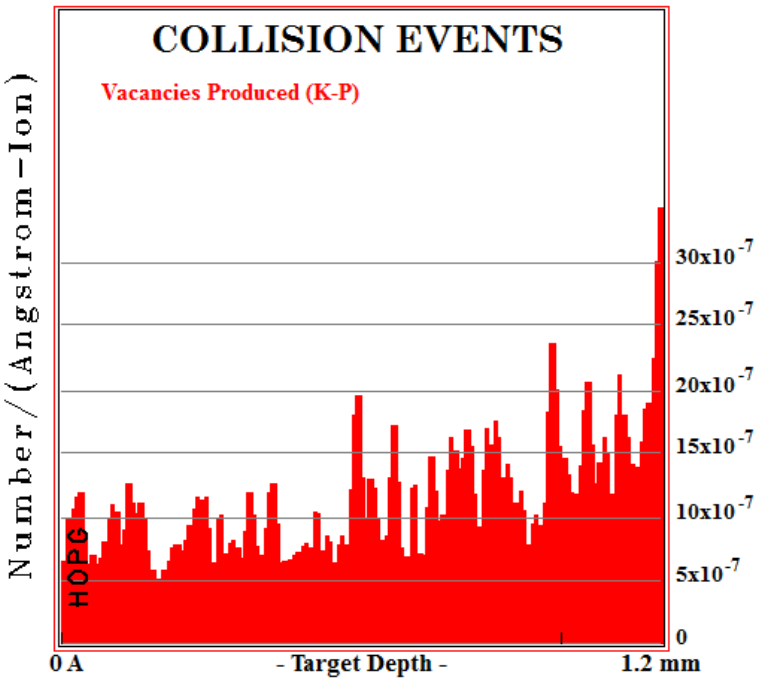

Figure 14 Displacement cross-section simulated by SRIM

So we further derive the equation for displacement cross-section (σ_d) is:

$$\sigma_d = \frac{Numbers\ of\ vacancies}{Ion-length\times number\ density} = \frac{Numbers\ of\ vacancy}{Ion-length} \times \frac{Atomic\ Number}{Carbon\ Density\times N_A} \tag{6}$$

The average numbers of vacancies per angstrom-ion simulated by SRIM, 13 can be used to calculate the displacement cross-section (σ_d). As a result, the dpa is 1.224×10^{-3} per hour. And Figure 15 shows the relationship between radiation time and dpa.

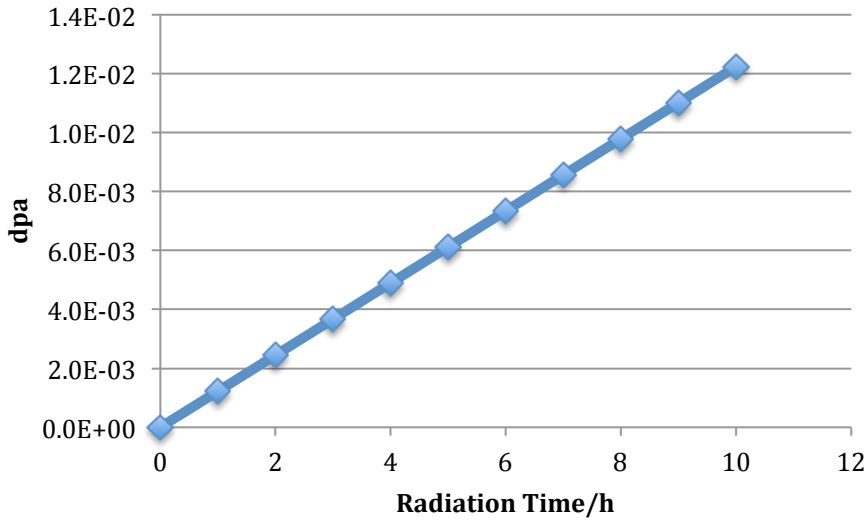

Figure 15 Graph of dpa at different radiation time

The method to measure the beamline current was introduced prior. Table 3 and Figure 16 shows the results of measured currents at different cyclotron current.

Table 3 Table of measured currents at different cyclotron current

Cyclotron current (μA)	Target current (μA)
10	0.34
15	0.47
20	0.59
25	0.76
30	0.89
35	1.07
40	1.22
45	1.34
50	1.47
55	1.58
60	1.79

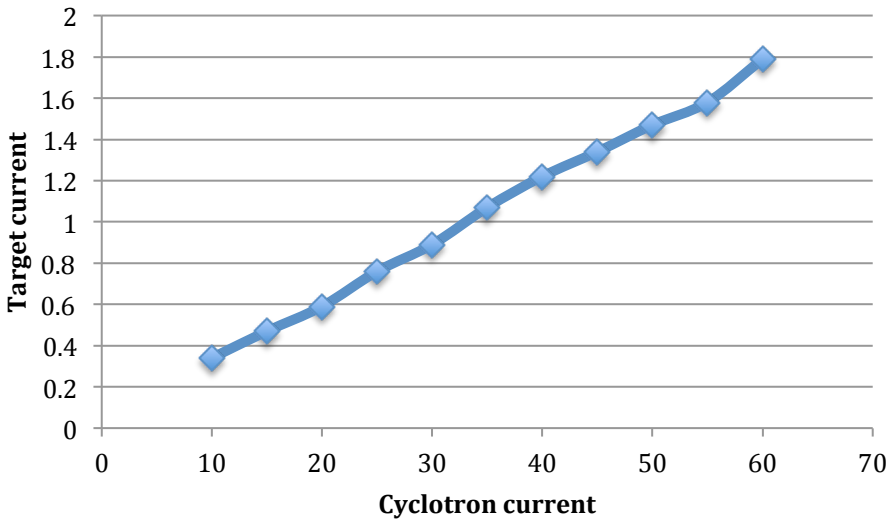

Figure 16 Graph of target beam current at different cyclotron

From the results shown in Table 3 and Figure 16, it is observed that the transfer rate of the current is 3%. The cyclotron emission current was 20μA measured at entrance to the beam line. And the beamline current at the material side is 0.6μA.

According to Tárkányi's method[17], the different ratio of ^{55}Co and ^{57}Ni indicates the different energy of beamline. Figure 17 shows the theoretical relationship between the ratio of ^{55}Co and ^{57}Ni and beamline energy and the nickel foil tested value of the ratio of ^{55}Co and ^{57}Ni.

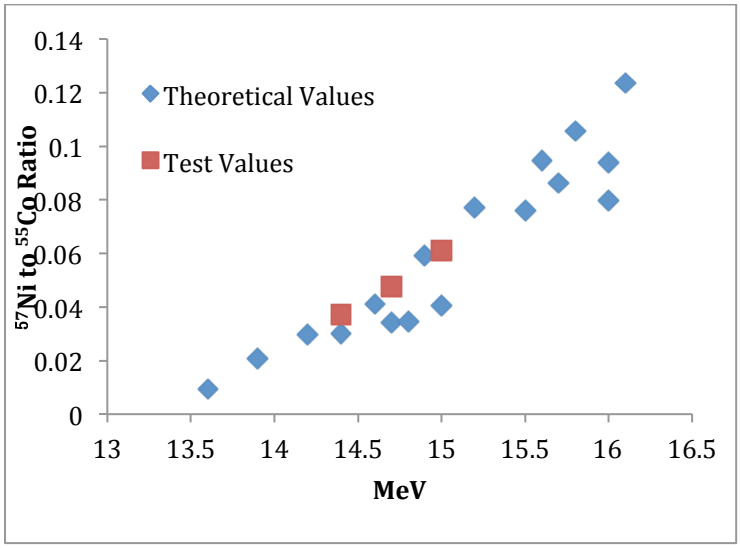

Figure 17 Theoretical and test values of the raio of ^{55}Co and ^{57}Ni

From the data, it can conclude that the beam energy is 14.7MeV ±0.3 MeV.

SEM provides a visual morphology of the graphite samples. Figure 18 is an SEM image of one of the samples. Figure 19 shows a SEM image of unirradiated sample. The layer structure on the unirradiated sample is caused by imperfectly cleave. Compared to the unirradiated sample, paralleled rod-shaped defects in the irradiated sample are observed. According to the multiple images acquired from different sample, these rod-shaped defects possess a mean length of 100μm and an average width of 10-20μm. That these paralleled rods seem to indicate that the damage effects are somehow very similar in a certain area[11].

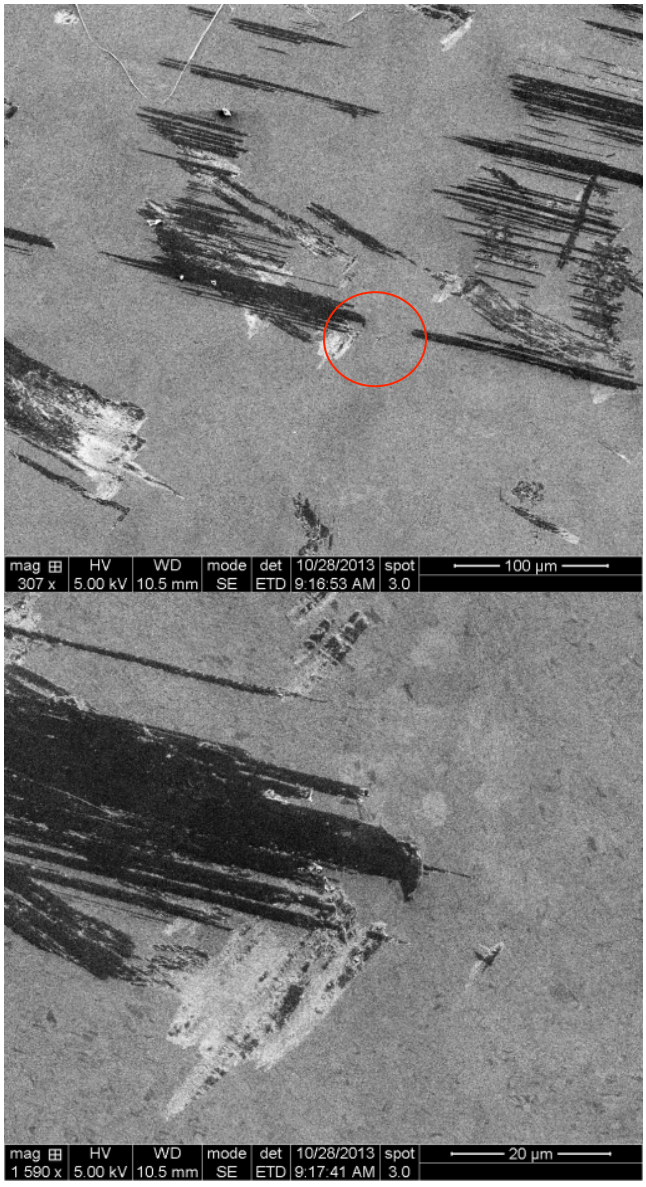

Figure 18 SEM images of the irradiated HOPG

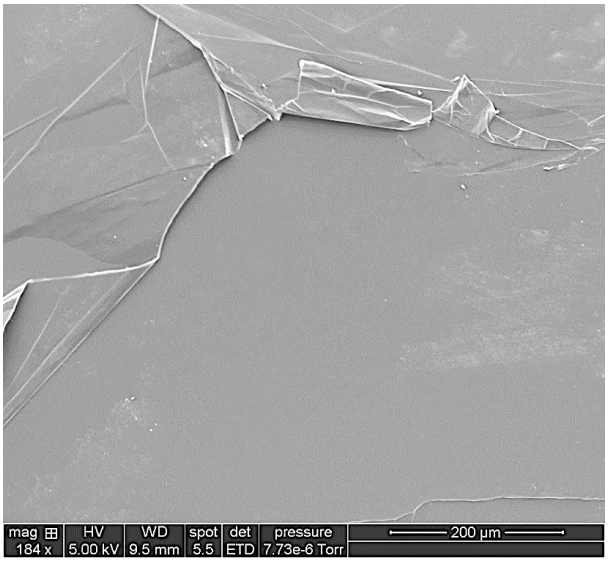

Figure 19 SEM image of the unirraidated HOPG

It is very hard to tell whether these rod-shaped defects are mountain-like or valley-like from the SEM image. AFM can be used to measure the height of the defects and portrait the surface topography of the sample. Figure 20 displays the AFM result of this defect structure. In order to better analyze the structure, three lines were drawn across the rod-shaped defect and get the line profiles of them at Figure 21. It also put in line profile information of an unirradiated sample to compare. The image of the unirradiated sample is not shown because almost everywhere at the unirradiated sample is as flat as it shown in Figure 21.

As a result, compared to the unirradiated sample, which is almost at the same height, the height at the location of the lines is about 100-150nm. These defects appear as mountain-liked (protrusions), rather than valley-liked.

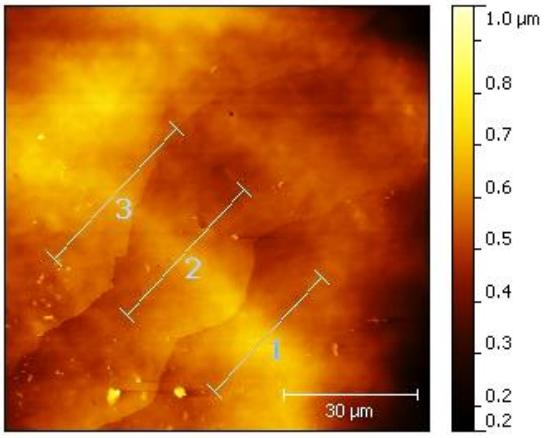

Figure 20 AFM image of rod-shaped defect

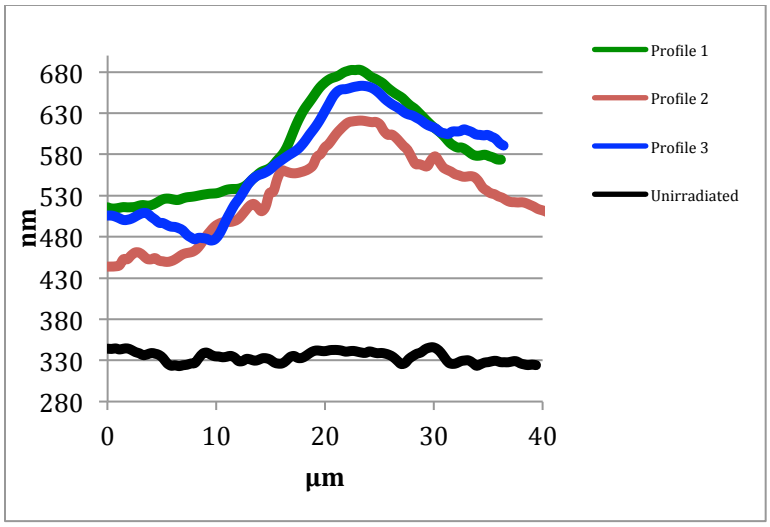

Figure 21 Profiles of 3 lines in 20 and a profile of unirradiated sample

It is possible that the dimensional change along the *c*-axis is caused by *Ruck and Tuck*. The layers underneath the mountain-liked rod-shaped defects are folded, which largely increase the dimension because the folded part multiplies the spacing within the structure. It was also found that the dimensional change at the center of the beamline and on the edge of the beamline is different. At the radiation center, the height of the defect is about 200-250nm while on the edge is about 100-150nm, as shown in Figure 22 and Figure 23. The higher the sample is, the more folded layers exist underneath the folded structure.

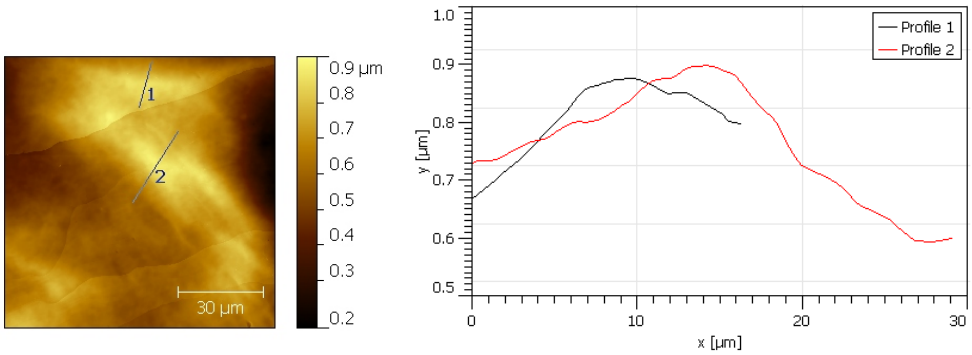

Figure 22 AFM image at the center of radiation area

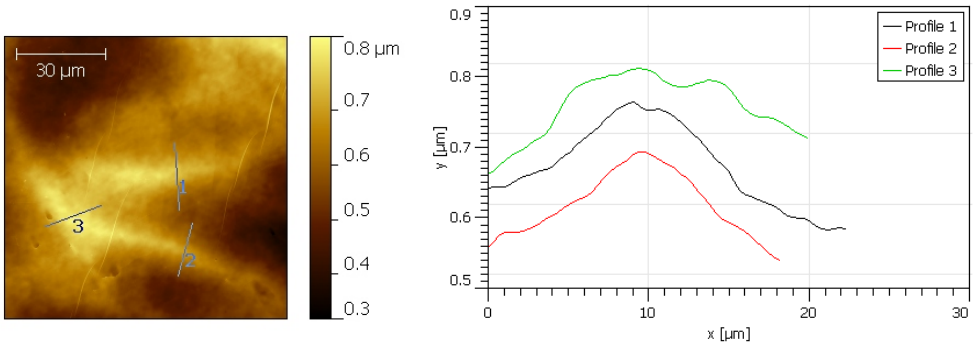

Figure 23 AFM images on the edge of the radiation area

The temperature and dpa distributions at different locations of the sample are different. One is not able to achieve the temperature and dpa distributions because there are still a lot of uncertainties in the radiation system. However, the different temperature and dpa on the sample is the main reason for the different height of the defect.

Although the sample is irradiated at the room temperature, some of the beam energy can be converted into heat during the irradiation. Because of the poor thermal conductivity of graphite along the *c*-axis, the heat will accumulate on the graphite and increase the temperature of the sample. At high temperature, the reaction rate of atoms being knocked out of their site is higher. And the dimensional changes are hard to anneal at high temperature, especially when the temperature is over 800ºC, 60% to 80% of the dimensional changes are unannealable[21]. It makes sense that at the center of the radiation area, the defect is more significant than on the edge of the radiation area.

FIB lift out sample will provide more intuitive evidence on the layer structures. Specimens were analyzed from the sample with HR-TEM, and the *ruck and tuck* structure was observed. The images are shown in Figure 24.

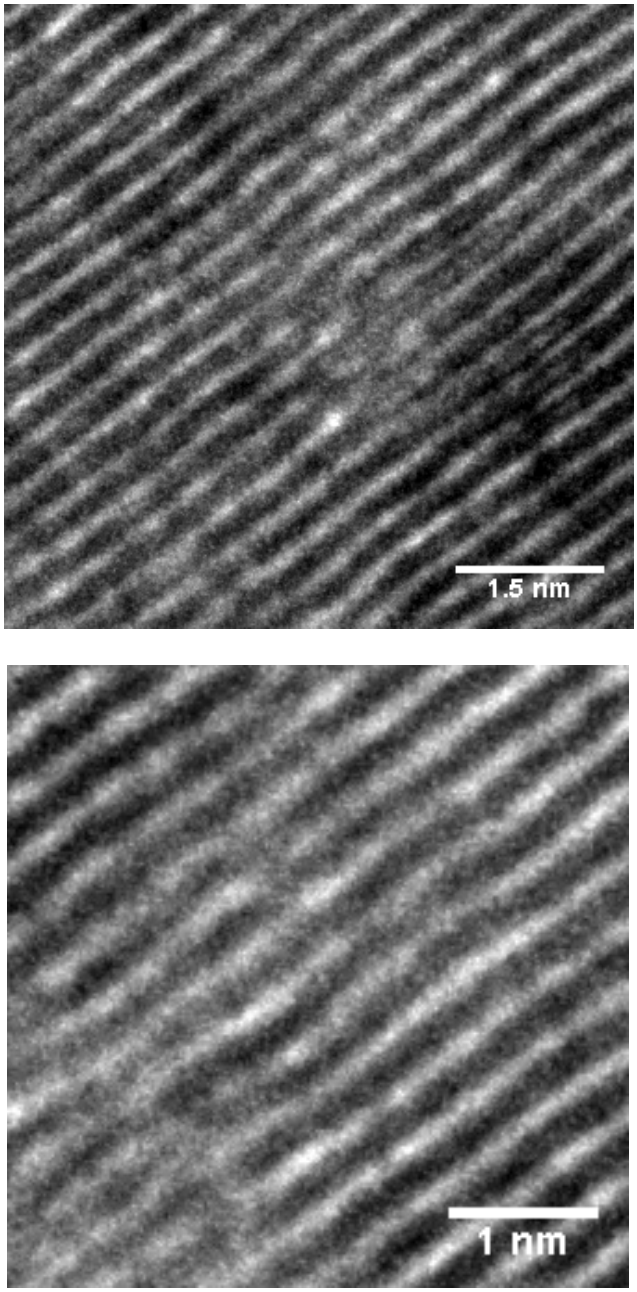

Figure 24 The image of ruck and tuck

From both images in Figure 24, the team observed the edge structure of *ruck and tuck*. In the above image, another two inserted layers are grown out at the spacing by the folded part. The increased spacing provides a place for interstitial clusters to be located and the inserted layer lowers the energy and creates a more stable structure[22]. Since it is a premature status of ruck and tuck structure, it's possible that before the folded layer could further increase its size, the interstitial clusters takes up the site and limits the ability of the folded structure to grow. In the second images of Figure 24, two adjacent folded

structures are observed. This is a mature status of *ruck and tuck*, which is stable and well developed.

It is observed that different heights exits between the center and the edge of the radiation area. It is possible to calculate the number of layers being folded underneath the rod-shaped defect. In order to calculate it, we made the following assumptions: 1) each folded layer does not possess another neighboring folded layer, which means the *ruck and tuck* structure does not emerge repeatedly between adjacent layers; and 2) each folded layer is long enough, so that we do not need to account for the edge geometries of these structures.

By recognizing the spacing between graphene layers in HOPG is 0.335nm and the thickness a graphite layer is 0.256nm, a rough estimation of the number of folded layers can be calculated as 85 to 125 layers on the edge and 170 to 210 layers at the center. However, it is still possible that several layers may fold together at the same place, like the second image in Figure 24, the actual number of folded layers will be less than the calculated value.

Figure 25 shows a HR-TEM image, in which dark spots with several nanometers in diameter and a few nanometers apart are observed. It was measured that the diameter of these dark spots and plot the percentage versus diameter in Figure 26. The mean diameter of these dark spots is 4nm, which is greater than a single dislocation defect but smaller than dislocation loops. After the single dislocation formed, especially in the context of interstitials which are more mobile than vacancies, that they are tending to coalesce with each other and form atomic clusters. Atomic clusters can further form dislocation loops. The size of atomic clusters is between that of a single interstitial, which is about 0.23nm in diameter, and an interstitial dislocation loop, which can be more than 30nm in size. As such, the observed dark spots are generically labled as atomic clusters.

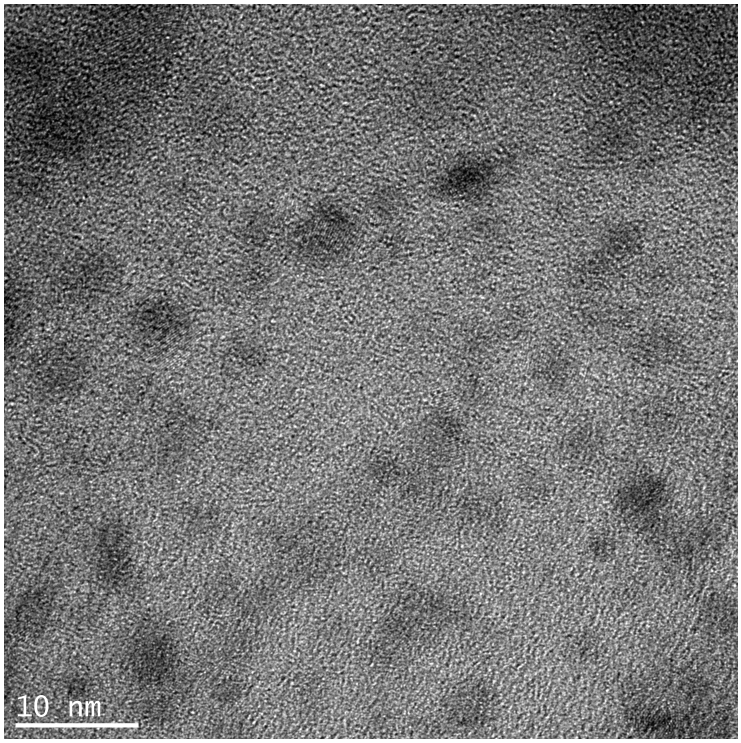

Figure 25 HR-TEM image of atomic cluster

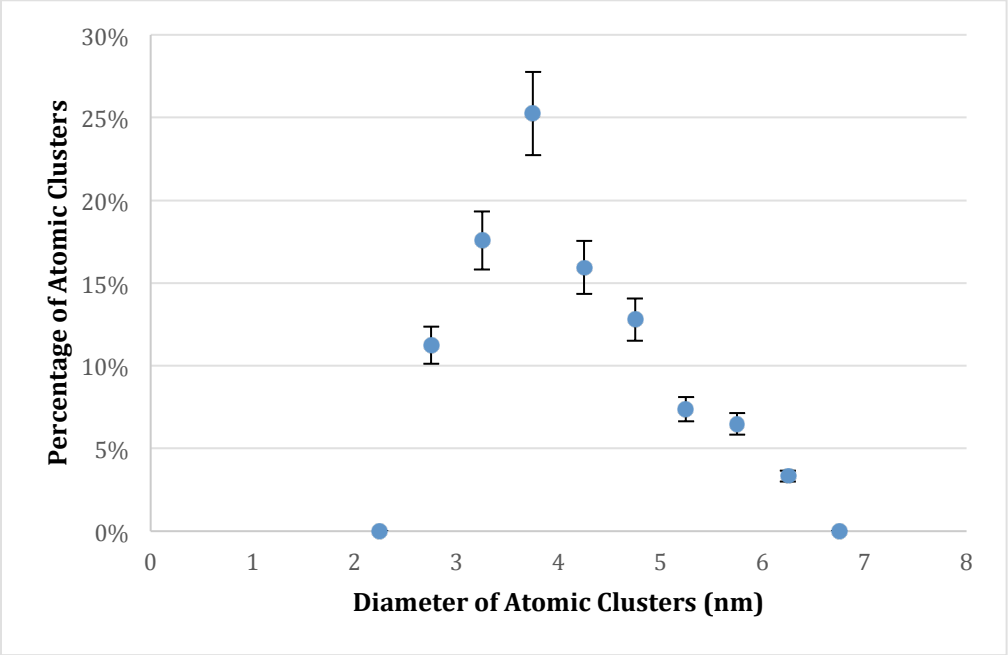

Figure 26 The distribution of atomic clusters

Atomic clusters are very hard to observe because their energy is high and not very stable. If they have energy to move and meet with another atomic cluster, they have a very high

possibility to coalesce with each other. The discovery of atomic clusters proves the theoretical radiation damage process.

Examples of TEM imaging on the irradiated sample are displayed in Figure 28. An unirradiated sample is shown in Figure 27 to be used to compare with irradiate sample. The unirradiated sample is multiple graphene layers. It shows that the way the sample was moved to the grid does not cause contrived damage onto the sample.

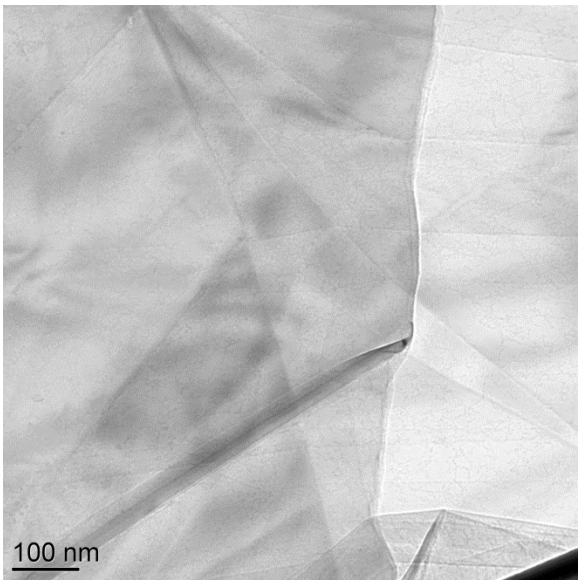

Figure 27 TEM image of unirradiated sample

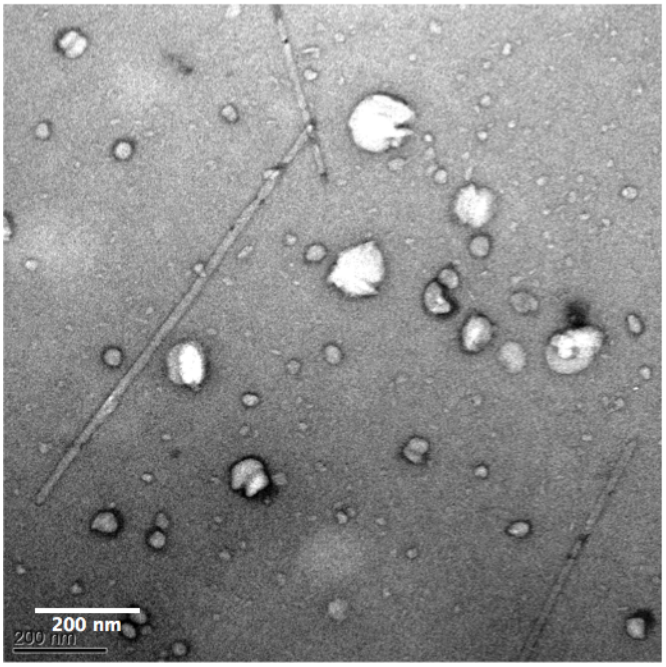

Figure 28 Image of Irradiated sample

Compared with TEM image of unirradiated graphite, the circular and hexagonal features found in the irradiated TEM images are dislocation loops cause by radiation. A graph comparing the percentage of dislocation loops of different diameters is shown in Figure 29. It was observed that samples of different radiation time have two major characteristic peaks. One of them is very consistent, which is around 20 nm; while the other varies between 30nm to 40nm. The smaller dislocation loops are vacancy dislocation loops while the greater ones are interstitial dislocation loops. The migration energy of interstitial is slightly smaller than the migration energy of vacancy, and the formation energy of interstitial is much smaller than the formation energy of vacancy. So the interstitial is more mobile which has higher chance to coalesce with other interstitial and further become bigger dislocation loops. Averaging the dislocation loop diameter data according to radiation dose, it was found that the average diameters of vacancy dislocation loops are 19.95nm. And the average diameter of interstitial dislocation loop is 40.18nm, 41.59nm and 39.32nm at 2 hour, 6 hour, and 9 hours, respectively. There is slightly different for the result of interstitial dislocation loops.

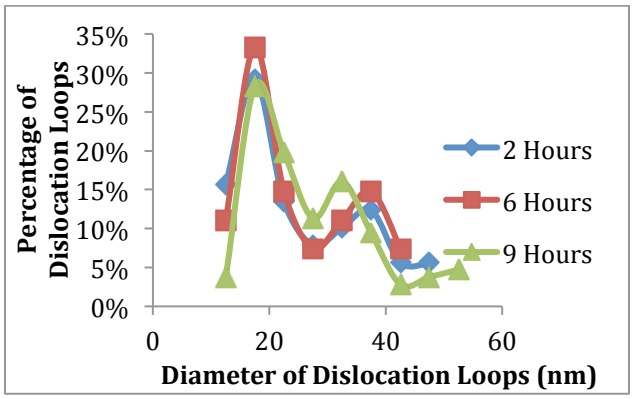

Figure 29 The distribution of dislocation loops

Based on current dpa, the 9 hour irradiated sample has a dpa of only 1.11×10^{-2}. The low dpa greatly limits the growth of dislocation loops. In the near future, we can increase the dpa by exposure the protons for longer times. Temperature is also an important factor in determining the size of radiation damage. Higher temperature may allow more damage effects to taken place.

REFERENCES:

[1] M. A. Fütterer, L. Fu, C. Sink, S. de Groot, M. Pouchon, Y. W. Kim, F. Carré, and Y. Tachibana, "Status of the very high temperature reactor system," *Prog. Nucl. Energy*, vol. 77, no. 0, pp. 266–281, 2014.

[2] R. Stainsby, K. Peers, C. Mitchell, C. Poette, K. Mikityuk, and J. Somers, "Gas cooled fast reactor research in Europe," 2011, 9th ed., vol. 241, pp. 3481–3489.

[3] G. B. Engle and B. T. Kelly, "Radiation Damage of Graphite in Fission and Fusion Reactor Systems," *J. Nucl. Mater.*, vol. 122, pp. 122–129, 1983.

[4] S. Humphries Jr, *Principles of charged particle acceleration*. Mineola, N.Y: Dover Publications, 2012.

[5] M. Beumer, "The Design & Construction of a Proton Microprobe Using a GE PETtrace Cyclotron." University of Missouri, 2012.

[6] Y. I. Shtrombakh, B. A. Gurovich, P. A. Platonov, and V. M. Alekseev, "Radiation damage of graphite and carbon-graphite materials," *J. Nucl. Mater.*, vol. 225, no. 1–3, pp. 273–301, 1995.

[7] R. H. Telling and M. I. Heggie, "Radiation defects in graphite," *Philos. Mag.*, vol. 87, no. 31, pp. 4797–4846, 2007.

[8] A. A. El-Barbary, R. H. Telling, C. P. Ewels, M. I. Heggie, and P. R. Briddon, "Structure and energetics of the vacancy in graphite," *Phys. Rev. B - Condens. Matter Mater. Phys.*, vol. 68, no. 14, pp. 1441071–1441077, 2003.

[9] V. Dubinko, A. Turkin, A. Abyzov, and M. Griffiths, "Modeling of the Simultaneous Evolution of Vacancy and Interstitial Dislocation Loops in hcp Metals Under Irradiation," *J. ASTM Int.*, vol. 3, no. 1, p. 18, 2006.

[10] M. I. Heggie, I. Suarez-Martinez, C. Davidson, and G. Haffenden, "Buckle, ruck and tuck: A proposed new model for the response of graphite to neutron irradiation," *J. Nucl. Mater.*, vol. 413, no. 3, pp. 150–155, 2011.

[11] H. Xiao, E. F. O. Donnell, and P. J. Pinhero, "Monitoring the Structural Change of Graphite under Fast Proton Radiation," *Trans. Am. Nucl. Soc.*, vol. 111, pp. 627–630, 2014.

[12] P. J. Zhai, Y. X. Xing, Y. Zhang, S. L. Feng, Y. X. Kang, X. W. Tang, Y. G. Wang, W. J. Zhao, and S. Yan, "Observation and study of latent tracks on the surface of HOPG induced by H+ ions," *Radiat. Meas.*, vol. 28, no. 1–6, pp. 97–100, 1997.

[13] V. S. Avilkina, N. N. Andrianova, A. M. Borisov, E. S. Mashkova, and E. S. Parilis, “Energy and temperature dependences of ion-induced electron emission from polycrystalline graphite,” *Nucl. Inst. Methods Phys. Res. B*, vol. 269, no. 9, pp. 995–998, 2011.

[14] T. D. Burchell, “Radiation effects in graphite and carbon-based materials,” *MRS Bull.*, vol. 22, no. 4, pp. 29–35, 1997.

[15] I. Strasik and M. Pavlovic, “Improvements to the SRIM simulations,” *Radiat. Eff. Defects Solids*, vol. 164, no. 7, pp. 470–476, 2009.

[16] J. F. Ziegler, M. D. Ziegler, and J. P. Biersack, “SRIM – The stopping and range of ions in matter (2010),” *Nucl. Inst. Methods Phys. Res. B*, vol. 268, no. 11, pp. 1818–1823, 2010.

[17] F. Tárkányi, F. Szelecsényi, and P. Kopecky, “Excitation functions of proton induced nuclear reactions on natural nickel for monitoring beam energy and intensity,” *Int. J. Radiat. Appl. Instrumentation. Part A. Appl. Radiat. Isot.*, vol. 42, no. 6, pp. 513–517, Jan. 1991.

[18] J. E. Sansonetti, “Handbook of Basic Atomic Spectroscopic Data,” *J. Phys. Chem. Ref. Data*, vol. 34, no. 4, p. 1559, 2005.

[19] R. B. Firestone and L. P. Ekström, “WWW Table of Radioactive Isotopes,” *LBNL Isotopes Project - LUNDS Universitet*, 2014. [Online]. Available: http://ie.lbl.gov/toi/.

[20] R. M. Langford and C. Clinton, “In situ lift-out using a FIB-SEM system.,” *Micron*, vol. 35, no. 7, pp. 607–11, Jan. 2004.

[21] J. . B. R.J Price, “Annealing of neutron-irradiated pyrocarbons,” *Carbon N. Y.*, vol. 9, no. 5, pp. 555–557, 1971.

[22] P. J. Ouseph, “Observation of prismatic dislocation loops in graphite by scanning tunneling microscope,” *Phys. Status Solidi Appl. Res.*, vol. 169, no. 1, pp. 25–32, 1998.